# A Wireless Power Transfer System With Dual Switch-Controlled Capacitors for Efficiency Optimization

Jianzhong Zhang, *Senior Member, IEEE*, Jin Zhao, *Student Member, IEEE*, Yaqian Zhang, and Fujin Deng, *Member, IEEE*

***Abstract*—This article proposes a novel wireless power transfer (WPT) system with switch-controlled capacitor (SCC) where variable capacitance and efficiency optimization are realized. The optimum asymmetrical voltage cancellation (OAVC) control is applied to realize wide-ranging soft-switching operation for the active bridge converters. The pulsewidth of the active bridge inverter regulates the output voltage, and the pulsewidth of the active bridge rectifier optimizes power delivery efficiency. The SCCs in the transmitter and the receiver sides are regulated for the zero-voltage switching operation and the resonant condition, respectively. The online estimation of mutual inductance is carried out to adapt the coupling deviations of the WPT system in real time. A 650-W prototype is built to verify the feasibility of the proposed WPT system and the effectiveness of the OAVC control. The experimental results show quite good performance and efficiency improvement for the WPT system at various loads.**

***Index Terms*—Dual active bridge, efficiency optimization, soft switching, switched capacitor, wireless power transfer (WPT).**

## I. Introduction

WIRELESS power transfer (WPT) technology has gained more and more attention due to the elimination of the restraint of the cable, which may provide safe, convenient, and effective power delivery for the equipment [1]–[3]. Today, the WPT has been widely adopted in industries and household appliances, such as electric vehicles [4]–[6], robots [7], mobile phones [8], and biomedical implants [9]. To reach a larger distance, a higher power rating and more efficient power delivery are the main trends for future WPT systems, and in recent years, substantial research works have been conducted on theoretical analysis, system optimization, and practical applications in various fields.

In the WPT system, the inductors and capacitors normally have quite large manufacturing tolerances and are easy to deviate from the nominal value due to the aging effect. Then, the resonant point can be influenced, which may cause additional apparent power and switching losses due to nonideal soft-switching state [10], [11]. This will lead to the reduction of efficiency for the power converter.

Therefore, it is challenging to keep the converter operating at the resonant condition under nonideal inductors and capacitors. The WPT system can be maintained resonant condition by utilization of variable capacitor and variable inductor to tune the resonant network [12]–[14].

However, even if the WPT systems operate at high efficiency under the resonant condition, the power delivery efficiency might still be not high enough because the maximum point of power efficiency only occurs under certain load impedance. Then, the load impedance should be converted to an optimum value to achieve high power delivery efficiency.

There are several schemes to solve these problems. In [15], an optimization of the compensation parameter is proposed to match the load impedance. This method cannot always convert the load impedance to the optimum value due to the load resistance varying with time in a practical system. An additional dc–dc converter is applied to adjust the equivalent impedance of the load to the optimum value in [16]–[18]. However, the converter costs a lot and introduces additional losses. An "ON–OFF keying" method is proposed in [20] which is applied to the converter of transmitter side. Then, the converter operates in "active mode" and "inactive mode" (ON–OFF) according to the load status. In this case, the WPT system may achieve high power delivery efficiency in a wide load range, but the maximum delivery efficiency is achieved only at the "active mode" and the delivery efficiency at the "inactive mode" is zero. Therefore, the average power delivery efficiency is low. An optimum asymmetrical voltage cancellation (OAVC) control is proposed in [21] for the converters to realize soft-switching operation. When compared to the phase shift and asymmetric duty cycle control proposed in [22]–[24], the OAVC control may expand the operation range of soft switching for the converter and could improve the efficiency performance of the WPT system.

In this article, a WPT system with switch-controlled capacitor (SCC) is proposed. The SCC technology was first proposed in [25] and it had been applied in various types of resonant converters to obtain constant frequency operation [26], [27]. The SCC had also been applied to the WPT systems [28], [29].

Manuscript received February 27, 2019; revised July 1, 2019 and September 16, 2019; accepted October 25, 2019. Date of publication November 5, 2019; date of current version February 20, 2020. This work was supported in part by the National Natural Science Foundation of China under Grant 51137001 and in part by the Foundation of Jiangsu Key Laboratory of Smart Grid Technology and Equipment. Recommended for publication by Associate Editor O. C. Onar. *(Corresponding author: Jianzhong Zhang.)*

The authors are with the School of Electrical Engineering, Southeast University, Nanjing 210096, China (e-mail: jiz@seu.edu.cn; zhaojin@seu.edu.cn; yaqianzhang83@163.com; fdeng@seu.edu.cn).

Color versions of one or more of the figures in this article are available online at http://ieeexplore.ieee.org.

Digital Object Identifier 10.1109/TPEL.2019.2950218

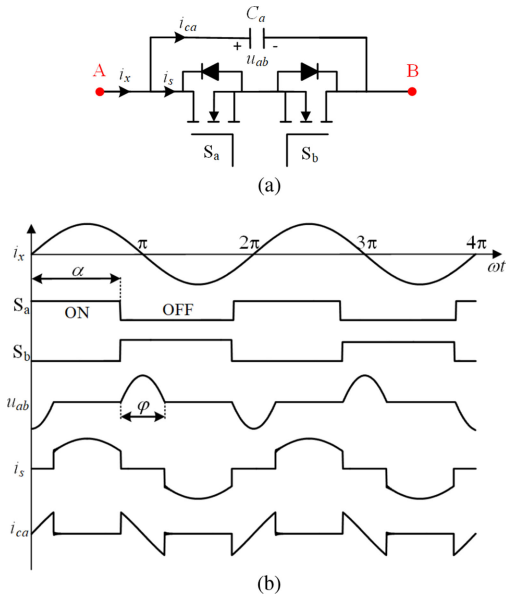


Fig. 1. SCC. (a) Structure. (b) Typical waveforms.

In [28], a pulsewidth modulation (PWM)-controlled capacitor was proposed to realize self-tuning of the *LCC* converter. Since the capacitance value was regulated by single switch with varied PWM ON/OFF duty ratio, the voltage stress will be high, and the range of variable capacitance was very small. In [29], the SCC was used as a primary-side capacitor to control the output power factor of the high-frequency inverter for minimizing the switching losses. However, the power delivery efficiency was not optimized. In the proposed WPT system of this article, the output voltage is adjusted by changing the pulsewidth of the inverter and optimum load impedance is matched by changing the pulsewidth of the rectifier. The SCCs in the transmitter and the receiver sides are regulated for zero-voltage switching (ZVS) operation and resonant condition, so that the system efficiency can be further improved.

This article is organized as follows. In Section II, the WPT system with dual SCCs is introduced and analyzed in detail. In Section III, the corresponding control strategy for the proposed system is discussed. The control strategy is implemented and validated by the experiments in Section IV. Finally, conclusions are drawn in Section V.

## II. WPT System With Dual SCC

### A. SCC

In this article, the fixed resonant capacitor is replaced by the SCC and the variable capacitance is realized for the efficiency optimization. Fig. 1(a) shows the structure of the SCC and it is composed of two source-to-source connected switches $S_a$, $S_b$, and a parallel linear capacitor $C_a$.

It is supposed that sinusoidal current $i_x$ $(x = 1, 2)$ is flowed through Terminals A and B, as shown in Fig. 1(a). The gate driving signals of the switches $S_a$ and $S_b$ are synchronized with current $i_x$. They have phase shift $\alpha$ from $i_x$ and are complementary each other. For a positive half-cycle, where $\pi/2 < \alpha < \pi$ and

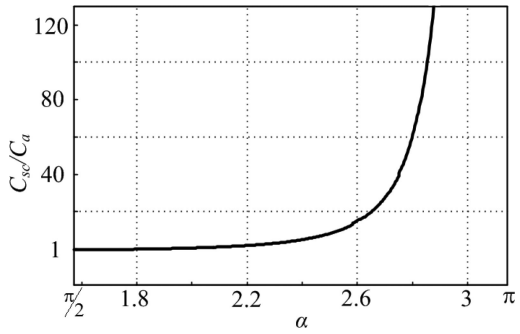


Fig. 2. Capacitance ratio $C_{\rm sc}/C_a$ versus phase angle shift $\alpha$.

the current flows from A to B, switch $S_a$ turns OFF at angle $\alpha$. Then, the current flows from A to B via capacitor $C_a$ and there is no current flowing through the switches. The current $i_x$ charges $C_a$ until $\pi$. The negative half-cycle begins at $\pi$ where the current flows from B to A and discharges capacitor $C_a$. After $C_a$ is fully discharged, the current flows from B to A via antiparallel diode of $S_a$.

Fig. 1(b) shows the voltage $u_{ab}$ which across Terminals A and B. This voltage is always zero at the instants when the stitches are turning ON and turning OFF, thus achieving the ZVS condition. Moreover, the antiparallel diodes of the switches begin to be reversely biased when switch has been or is turned ON, thus minimizing the effect of reverse recovery current. Therefore, the switching losses in this type of SCC are fairly low and the SCC could be applied in high-frequency applications which may reach megahertz range. However, there has a limitation for the SCC in higher frequency implications due to zero-crossing detection delay. It should point out that low on-state resistance of the switches (MOSFETs) should be selected for minimizing the conduction power losses, which may improve the performance in high-frequency implications.

The positive part of $i_s$ is the current flowed through switch $S_a$ while the negative part is the current flowed through $S_b$. The voltage drop across Terminals A and B is limited by capacitor $C_a$ and is proportional to the integration of the current flowed through the capacitor $C_a$. When phase shift $\alpha$ is changed from $\pi/2$ to $\pi$, the equivalent capacitance is modulated from $\infty$ to $C_a$. If the harmonics higher than second order are neglected, the equivalent capacitance $C_{\rm sc}$ of the SCC is derived as (1). The detail derivation process is shown in Appendix I

$$C_{\rm sc} = \frac{\pi C_a}{2\pi - 2\alpha + \sin 2\alpha}. \tag{1}$$

As shown in Fig. 2, the capacitance ratio of $C_{\rm sc}/C_a$ with respect to the phase angle shift $\alpha$ could be obtained using (1). Obviously, the equivalent capacitance $C_{\rm sc}$ can be modulated effectively by changing the phase angle shift $\alpha$. Fig. 2 shows that the capacitance ratio $C_{\rm sc}/C_a$ equals 1 at the point of $\alpha = \pi/2$. At this point, capacitor $C_a$ is always connected in the circuit and the current flows from Terminals A to B continuously. The switches $S_a$ and $S_b$ switch OFF all the time, and there is no current going through these two switches. When the phase angle shift $\alpha$ equals $\pi$, there would be no current flowing through the capacitor $C_a$. Capacitor $C_a$ is always short-circuited by the switches. In

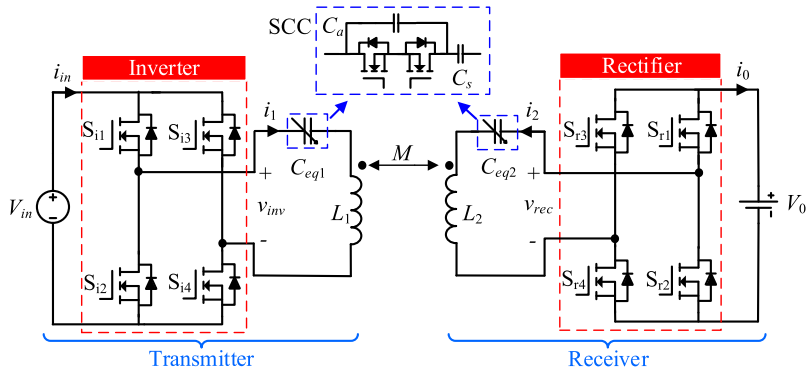


Fig. 3. WPT system with dual SCCs.

this case, capacitor is equivalent to a short-circuited line and its equivalent capacitance is infinite.

### *B. Proposed WPT System With SCC*

The proposed WPT system with dual SCCs has a symmetrical structure, as shown in Fig. 3. It consists of an active bridge inverter, an active bridge rectifier, coupled coils, two series capacitors, and two SCCs. Each SCC is connected in series with a capacitor $C_s$ to modulate the equivalent resonant capacitance by controlling the phase angle $\alpha$.

The power is transferred from the transmitter coil to the receiver coil with the coupling factor *k*, which can be defined as

$$k = \frac{M}{\sqrt{L_1 L_2}} \tag{2}$$

where *M* is the mutual inductance, and $L_1$ and $L_2$ are the inductance of the transmitter coil and the receiver coil, respectively. The transmitter resonance frequency $\omega_1$, the receiver resonance frequency $\omega_2$, the transmitter reactance $X_1$, and the receiver reactance $X_2$ are defined as

$$\begin{aligned} &\omega_1 = \frac{1}{\sqrt{L_1 C_{\mathrm{eq1}}}}, \omega_2 = \frac{1}{\sqrt{L_2 C_{\mathrm{eq2}}}}, \\ &X_1 = \omega L_1 - \frac{1}{\omega C_{\mathrm{eq1}}}, X_2 = \omega L_2 - \frac{1}{\omega C_{\mathrm{eq2}}} \end{aligned} \tag{3}$$

where $C_{\mathrm{eq1}}$ and $C_{\mathrm{eq2}}$ are the equivalent capacitance of the series capacitor $C_s$ and the SCC.

### *C. Analysis of WPT System*

As shown in Fig. 4(a), a fundamental harmonic analysis model of the WPT system is studied to analyze the characteristics of the proposed WPT system. The equivalent series resistances (ESRs) $R_1$ and $R_2$ are used to stand for the power losses, such as the conduction loss of the coils and switches, the switching loss and the radiation loss. In the proposed WPT system, the losses introduced by the coils and the SCC operation are very small. To simplify the analysis, we assume $R_1$ and $R_2$ are constant. $R_{\mathrm{eq}}$ is the equivalent ac load resistance, which equals the input resistance of the high-frequency rectifier.

The current-controlled voltage source (CCVS) is used to indicate the effect of the mutual inductance voltage, and then the

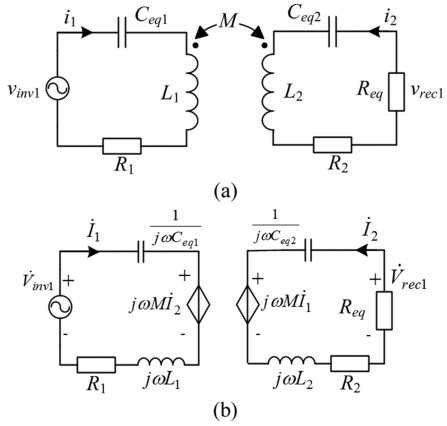


Fig. 4. Equivalent circuit. (a) Fundamental harmonic analysis model. (b) Equivalent decoupling circuit.

equivalent circuit is decoupled by CCVS, as shown in Fig. 4(b). According to Kirchhoff's voltage law, the voltage equations of the WPT system are

$$\begin{cases} (R_1 + jX_1)\dot{I}_1 + j\omega M\dot{I}_2 = \dot{V}_{\mathrm{inv1}} \\ j\omega M\dot{I}_1 + (R_2 + R_{\mathrm{eq}} + jX_2)\dot{I}_2 = 0 \\ R_{\mathrm{eq}}\dot{I}_2 = -\dot{V}_{\mathrm{rec1}} \end{cases} \tag{4}$$

where $\dot{V}_{\mathrm{inv1}}$ and $\dot{V}_{\mathrm{rec1}}$ are the phasors of fundamental ac input voltage and output voltage, respectively; $\dot{I}_1$ and $\dot{I}_2$ are phasors of the inductor current, *j* is the imaginary unit; and $\omega$ is operation frequency of the WPT system. The voltage gain can be defined as

$$G_v = \frac{\dot{V}_{\mathrm{rec1}}}{\dot{V}_{\mathrm{inv1}}} = \frac{j\omega M R_{\mathrm{eq}}}{(jX_1 + R_1)(jX_2 + R_2 + R_{\mathrm{eq}}) + (\omega M)^2}. \tag{5}$$

In order to achieve high power delivery efficiency, the operating frequency $\omega$ of the WPT system should be the same as the resonant frequency $\omega_2$ of the receiver, and then it has $X_2 = 0$. In this case, the voltage gain $|G_v|$ can be obtained according to Table I and (9), as shown in Fig. 5. Here $X_2$ is set to be zero and $X_1$ is set in the range from –10 to 10 Ω. It is shown that voltage gain $|G_v|$ increases when load resistance increases. For a fixed

TABLE I
PARAMETERS OF THE WPT SYSTEM FOR ANALYSIS

| Symbol | Parameter | Value |
|---|---|---|
| $f$ | Operating frequency | 100 kHz |
| $L_1$ | Transmitter coil inductance | 100 $\mu$H |
| $L_2$ | Receiver coil inductance | 100 $\mu$H |
| $R_1$ | ESR of transmitter side | 0.4 Ω |
| $R_2$ | ESR of receiver side | 0.4 Ω |
| $M$ | Mutual inductance | 34 $\mu$H |
| $R_{\rm eq}$ | Equivalent ac load resistance | [1, 100] Ω |
| $X_1$ | Transmitter reactance | [–10, 10] Ω |
| $X_2$ | Receiver reactance | [–15, 15] Ω |

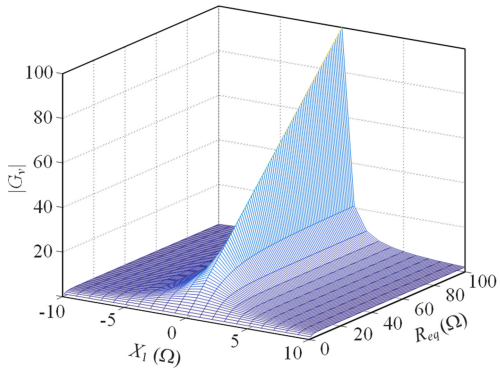


Fig. 5. Voltage gain $G_v$ against equivalent resistance $R_e$ and reactance $X_1$.

load resistance, voltage gain $|G_v|$ decreases when transmitter resistance increases.

Considering the soft-switching condition for the inverter, $X_1$ normally does not equal zero ($X_1 \neq 0$) which means that the transmitter side works on the nonresonance state. Thus, the inverter should have an inductive load to achieve ZVS when $X_1 > 0$. In this case, a reduction of the voltage gain will occur as the voltage gain is decreased according to the increasing of $X_1$, as shown in Fig. 5.

The efficiency of the WPT system can be defined based on the input power and the output power and it has

$$\eta = \frac{P_{\rm out}}{P_{\rm in}} = \frac{{\rm Re}[-\dot{V}_{\rm rec1}\dot{I}_2^*]}{{\rm Re}[\dot{V}_{\rm inv1}\dot{I}_1^*]} = \frac{\omega^2 M^2 R_{\rm eq}}{\omega^2 M^2 (R_2 + R_{\rm eq}) + R_1((R_2 + R_{\rm eq})^2 + X_2^2)}. \quad (6)$$

It is shown that the efficiency $\eta$ is a function of the reactance $X_2$ and the equivalent resistance $R_{\rm eq}$, as shown in Fig. 6. For a fixed equivalent load $R_{\rm eq}$, the efficiency $\eta$ decreases with the increase of $|X_2|$. The existence of additional reactance $X_2$ causes a larger apparent power, resulting in a lower efficiency. Thus, higher $|X_2|$ will lead to lower efficiency $\eta$. The efficiency $\eta$ can achieve the peak value when $X_2 = 0$. However, the efficiency $\eta$ keeps varying with the equivalent load $R_{\rm eq}$. It is obvious that the efficiency has an optimal load resistance (OLR) for achieving

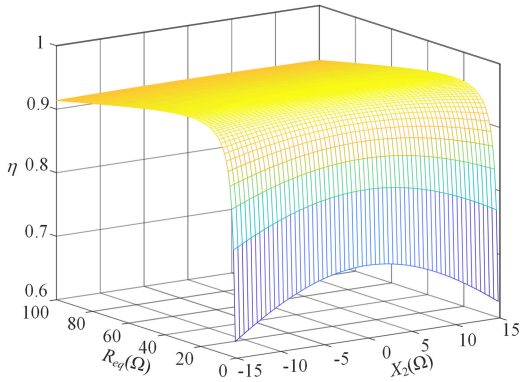


Fig. 6. Efficiency against equivalent resistance $R_{\rm eq}$ and reactance $X_2$.

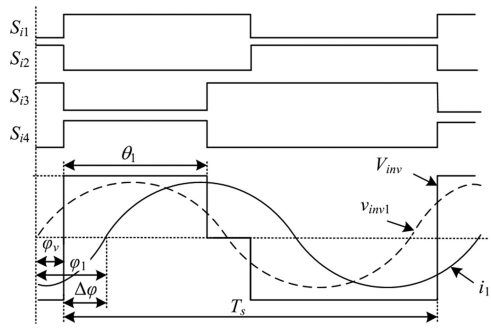


Fig. 7. Typical waveforms of inverter under the OAVC control.

maximum value. The OLR can be derived by

$$\frac{d\eta}{dR_{\rm eq}}|_{X_2=0} = 0. \quad (7)$$

Then, the OLR $R_{\rm eq}^{\rm opt}$ is calculated as

$$R_{\rm eq}^{\rm opt} = R_2\sqrt{1 + \frac{\omega^2 M^2}{R_1 R_2}}. \quad (8)$$

According to (8), $R_{\rm eq}^{\rm opt}$ is the function of $R_1$, $R_2$, and $M$ at fixed operating frequency $\omega$. The equivalent load $R_{\rm eq}$ of the receiver side should be maintained as closely as possible to the OLR $R_{\rm eq}^{\rm opt}$ to achieve high efficiency.

## III. CONTROL STRATEGIES

The OAVC control is applied to the dual active bridge converters in order to realize a wide-range soft-switching operation. Fig. 7 shows the typical waveforms of the OAVC control for the inverter in the transmitter side, where $S_{i1}$–$S_{i4}$ are the drive signal of switches, $V_{\rm inv}$ is the quasi-square output voltage, and $i_1$ is the output current of the inverter bridge. The dashed waveform $v_{\rm inv1}$ is the fundamental component of $V_{\rm inv}$. One switch pair ($S_{i1}$, $S_{i2}$) is always operated complementarily at the fixed duration angle $\pi$ during one switching period $T_s$, and another switch pair ($S_{i3}$, $S_{i4}$) is complementarily operated at turn-OFF angle $\theta_1$ during one-half switching period $T_s$.

The fundamental component of the quasi-square output voltage $V_{\rm inv}$ can be expressed as

$$v_{\rm inv1} = V_{\rm inv1}\sin(\omega t+\phi_v) = \frac{V_{\rm in}}{\pi}\sqrt{10-6\cos\theta_1}\sin(\omega t+\phi_v) \tag{9}$$

where $V_{\rm in}$ is the dc input voltage, $V_{\rm inv1}$ and $\varphi_v$ are the amplitude and phase angle of the fundamental component of $V_{\rm inv}$, respectively. The rms value of $v_{\rm inv1}$ is

$$V_{\rm inv1\_rms} = \frac{V_{\rm inv1}}{\sqrt{2}} = \frac{V_{\rm in}}{\pi}\sqrt{5-3\cos\theta_1}. \tag{10}$$

The phase angle $\varphi_v$ can be expressed as

$$\phi_v = \arctan\frac{\sin\theta_1}{3-\cos\theta_1}. \tag{11}$$

### A. Voltage Regulation in Inverter

The voltage regulation can be realized by adjusting the pulsewidth $\theta_1$ of the inverter, as shown in Fig. 7. The desired pulsewidth $\theta_1$ for voltage regulation can be derived as (12). The detailed derivation processes are shown in Appendix II

$$\theta_1 = \arccos\left[\frac{1}{3}\left(5-\frac{\pi^2V_0^2}{V_{\rm in}^2}\times\frac{\left((R_1(R_2+R_{\rm eq})+(\omega M)^2\right)^2+X_1^2(R_2+R_{\rm eq})^2\right)}{(\omega M)^2R_{\rm eq}R_L}\right)\right]. \tag{12}$$

As shown in (12), the pulsewidth $\theta_1$ could be calculated according to the required output voltage $V_0$. The voltage regulation can be achieved by adopting a different pulsewidth of $\theta_1$.

### B. Soft-Switching Condition

The phase angle $\alpha_1$ of the SCC in the transmitter side could be adjusted to achieve ZVS operation of the inverter, and controllable equivalent capacitance $C_{\rm eq1}$ is thereby obtained. Furthermore, the controllable equivalent capacitance $C_{\rm eq1}$ can partially compensate the reactance of the transmitter coil. The equivalent impedance in the transmitter side is

$$Z_{\rm in} = R_1 + jX_1 + Z = R_1 + jX_1 + \frac{\omega^2M^2}{R_2+R_{\rm eq}} \tag{13}$$

where $Z_{\rm in}$ is the equivalent impedance in the transmitter side, $Z$ is the reflected impedance from the receiver side to the transmitter side and is pure resistance when the operating frequency is in resonance with $C_{\rm eq2}$ in the receiver side.

The phase angle delay $\varphi_1$ (see Fig. 7) between $V_{\rm inv1}$ and $i_1$ of the fundamental component can be expressed as

$$\phi_1 = \arctan\frac{X_1}{R_1+Z} = \arctan\left(Q\left(\omega_n-\frac{1}{\omega_n}\right)\right) \tag{14}$$

where $Q=\sqrt{L_1/C_{\rm eq1}}/(R_1+Z)$, $\omega_n=\omega/\omega_1$, and $\omega_1 = 1/\sqrt{L_1C_{\rm eq1}}$.

In order to realize the ZVS operation for the inverter, the current $i_1$ should go through the antiparalleled diode before triggering the power switches, meaning that $Z_{\rm in}$ needs to be inductive to form a lagging current. Therefore, the necessary condition of ZVS for power switches can be obtained from (14) and (19) by setting $\varphi_1$–$\varphi_v = \Delta\varphi > 0$, it is

$$Q\left(\omega_n-\frac{1}{\omega_n}\right) \ge \frac{\sin\theta_1}{3-\cos\theta_1}. \tag{15}$$

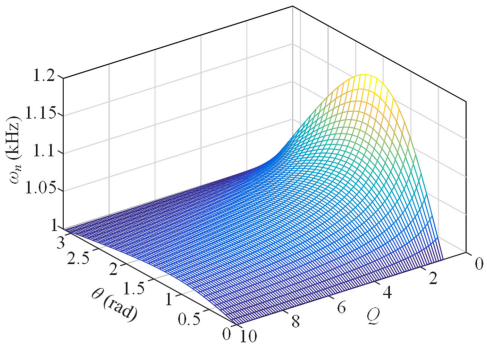


Fig. 8. Minimum $\omega_n$ required for ZVS versus pulsewidth $\theta_1$ and factor $Q$.

In order to achieve ZVS operation, the current of the inverter should lag a little behind the voltage. Then, the inverter should have an inductive load, which means $X_1 > 0$. In this case, $\omega_n > 1$ is necessary. In order to satisfy (15), $\omega_n$ can be increased. In traditional methods, this increase is realized by increasing the operating frequency $\omega$. However, it is not suitable for constant frequency operations where $\omega$ is fixed. In this study, $\omega_n$ is regulated by reducing the resonant frequency $\omega_1$, which is achieved by the SCC in order to changing the equivalent capacitance $C_{\rm eq1}$. It should be noted that larger $\omega_n$ will result in a large reactive current, which will in turn lead to a better reduction of the voltage gain $|G_v|$. Therefore, one of the goals of the control strategy is to minimize $\omega_n$ while maintaining the ZVS operation. As shown in Fig. 8, the minimum value of $\omega_n$ ($\omega_{n\_\min}$) for the ZVS operation could be obtained based on (15).

The ZVS operation can be realized by meeting the inequality constraint of (15). If the right side of (15) reaches the maximum value, which is the worst case for the conditions of the ZVS operation, the operation will be guaranteed in all range of load variations. In order to find the maximum value, the right side of (15) is treated as

$$\frac{\partial}{\partial\theta_1}\left(\frac{\sin\theta_1}{3-\cos\theta_1}\right) = 0. \tag{16}$$

The right side of the inequality can achieve the maximum value at $\cos\theta_1 = 1/3$. The quality factor $Q$ greatly influences on the ZVS operation, and the larger $Q$ leads to higher voltage stresses in the resonant components. On the other hand, a small $Q$ makes the inverter operate under low efficiency due to the high circulation current and high-order harmonics.

Synthesizing (15) and (16), $\omega_{n\_\min}$ can be calculated as

$$\omega_{n\_\min} = \frac{1}{8}\frac{\sqrt{2}+\sqrt{64Q^2+2}}{Q} \tag{17}$$

where $\omega_{n\_\min}$ is the minimum value of $\omega_n$. As shown in Fig. 3, the SCC is connected in series with capacitor $C_s$. Considering equivalent capacitance $C_{\rm sc}$ of the SCC, the total equivalent

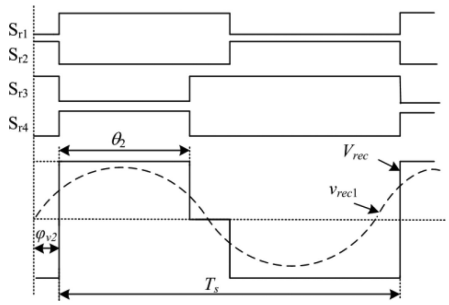


Fig. 9. Typical waveforms of rectifier under the OAVC control.

capacitance $C_{\mathrm{eq1}}$ is

$$C_{\mathrm{eq1}} = \frac{C_{\mathrm{sc}}C_s}{C_{\mathrm{sc}}+C_s} = \frac{\pi C_a C_s}{\pi C_a + 2\pi C_s - 2\alpha_1 C_s + C_s \sin(2\alpha_1)} \tag{18}$$

where $\alpha_1$ is the phase shift angle of the SCC in the transmitter side and $\alpha_1 \in [\pi/2,\pi]$. The minimum equivalent capacitance $C_{\mathrm{eq1\_min}}$ is determined in (19) by the minimum $\omega_{n\_\min}$ at the worst case for the ZVS operation

$$C_{\mathrm{eq1\_min}} = \frac{\omega_{n\_\min}^2}{\omega^2 L_1}. \tag{19}$$

### C. OLR Control in Rectifier

The reactance of the receiver side can be compensated by adjusting the phase angle $\alpha_2$ of the SCC and varying the equivalent capacitance $C_{\mathrm{eq2}}$ in receiver side. Therefore, the operating frequency can be adjusted in resonance with $C_{\mathrm{eq2}}$, and the phase angle $\alpha_2$ of the SCC in the receiver side can be calculated by setting $X_2 = 0$. The OLR $R_{\mathrm{eq}}^{\mathrm{opt}}$ at the maximum efficiency point can be achieved by adjusting the pulsewidth $\theta_2$ of the rectifier.

The input voltage of the rectifier $V_{\mathrm{rec}}$ is regulated by the pulsewidth $\theta_2$, as shown in Fig. 9. Similar to (13), the fundamental component of voltage $V_{\mathrm{rec}}$ can be expressed as

$$v_{\mathrm{rec1}} = \frac{V_0}{\pi}\sqrt{10 - 6\cos\theta_2}\sin(\omega t + \phi_{v2}) \tag{20}$$

where $V_0$ and $\theta_2$ are the dc output voltage of the load and the pulsewidth of $V_{\mathrm{rec}}$, respectively, $\varphi_{v2}$ is the phase angle of the fundamental component of $V_{\mathrm{rec}}$.

The root mean square (rms) value of $v_{\mathrm{rec1}}$ is

$$V_{\mathrm{rec1\_rms}} = \frac{V_0}{\pi}\sqrt{5 - 3\cos\theta_2}. \tag{21}$$

The current of receiver coil $i_2$ can be expressed as

$$i_2 = \sqrt{2} I_{2\_\mathrm{rms}} \sin(\omega t + \phi_{v2}) \tag{22}$$

where $I_{2\_\mathrm{rms}}$ is the rms value of $i_2$. Therefore, the dc output current $I_0$ can be expressed as

$$I_0 = \frac{2}{Ts}\int_0^{\frac{T_s}{2}} |i_2(t)|dt = \frac{I_{2\_\mathrm{rms}}}{\pi}\sqrt{5 - 3\cos\theta_2}. \tag{23}$$

Since $V_{rec1\_\mathrm{rms}}$ and $I_{2\_\mathrm{rms}}$ are in phase by setting the rectifier in the resonant state and $X_2 = 0$, the equivalent ac load resister $R_{\mathrm{eq}}$ is

$$R_{\mathrm{eq}} = \frac{V_{\mathrm{rec1\_rms}}}{I_{2\_\mathrm{rms}}} = \frac{R_L}{\pi^2}(5 - 3\cos\theta_2) \tag{24}$$

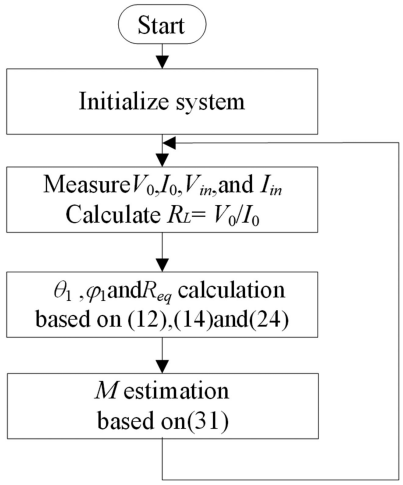


Fig. 10. Estimation of mutual inductance $M$.

where $R_L$ is resistance of the load and is defined as $R_L = V_0/I_0$. When $\theta_2 = \pi$, the rectifier operates at synchronous rectifying. Thus, (24) can be simplified as

$$R_{\mathrm{eq}} = \frac{8}{\pi^2}R_L. \tag{25}$$

An OLR exists for the maximum efficiency of the WPT system, which can be regulated by adjusting the pulsewidth of the rectifier. Supposing that $R_{\mathrm{eq}}^{\mathrm{opt}}$ is the OLR at the maximum efficiency point, the desired pulsewidth $\theta_2$ of the rectifier can be derived from (8) and (24) as

$$\theta_2 = \arccos\left[\frac{1}{3}\left(5 - \frac{\pi^2 R_2}{R_L}\sqrt{1 + \frac{(\omega M)^2}{R_1 R_2}}\right)\right]. \tag{26}$$

As shown in (25), the pulsewidth $\theta_2$ could be calculated according to the resistance of the load $R_L$. By adopting the pulsewidth $\theta_2$, the OLR $R_{\mathrm{eq}}^{\mathrm{opt}}$ at the maximum efficiency point can tracked dynamically. Thus, the efficiency can be maintained constant at any load occasion.

### D. Mutual Inductance Estimation

Equations (12) and (26) show that the variable $\theta_1$ and $\theta_2$ are adopted to regulate the output voltage and the OLR, which are both related to the mutual inductance $M$. However, the mutual inductance may vary because of the different position between the transmitter and receiver coils. Therefore, it is necessary to estimate the mutual inductance for the coupled coils in real time. The proposed online mutual inductance estimation is based on dc voltage and current sampling, and it is easy to implement.

According to (9), the voltage $\dot{V}_{\mathrm{inv1}}$ leads the current $\dot{I}_1$ by $\varphi_1$. Then, it has

$$\frac{V_{\mathrm{inv1}}}{I_1}e^{j\phi_1} = R_1 + \frac{(\omega M)^2}{R_2 + R_{\mathrm{eq}}} + jX_1 \tag{27}$$

where $V_{\mathrm{inv1}}$ and $I_1$ are the rms value of phasors $\dot{V}_{\mathrm{inv1}}$ and $\dot{I}_1$, respectively. Equation (27) can be decomposed into two parts,

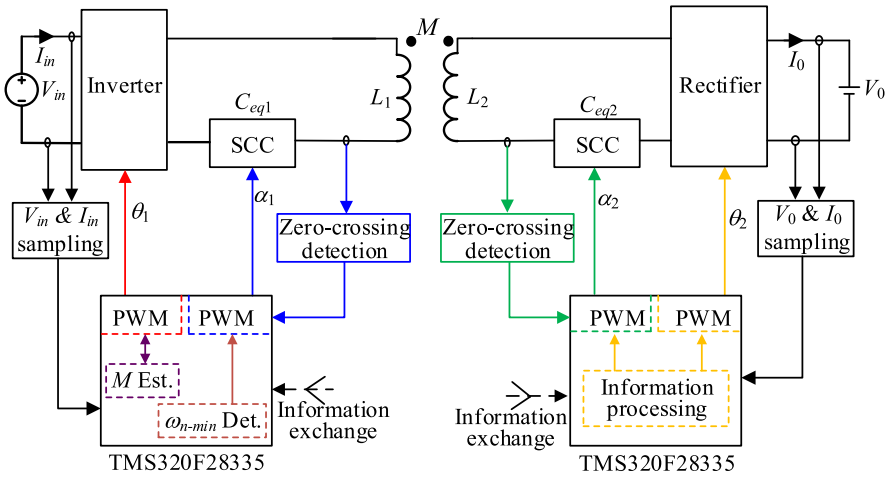


Fig. 11. Implementation of the WPT system.

which are

$$\frac{V_{\text{inv1}}}{I_1}\cos\phi_1 = R_1 + \frac{(\omega M)^2}{R_2 + R_{\text{eq}}} \tag{28}$$

$$\frac{V_{\text{inv1}}}{I_1}\sin\phi_1 = X_1. \tag{29}$$

Considering that the input power and output power of the inverter should be equal, it has

$$V_{\text{in}} I_{\text{in}} = V_{\text{inv1}} I_1 \cos\phi_1. \tag{30}$$

According to (9), (28), and (30), the estimated $M$ can be derived as

$$M = \sqrt{\frac{(V_{\text{in}}(5 - 3\cos\theta_1)\cos^2\phi_1 - \pi^2 I_{\text{in}} R_1)(R_2 + R_{\text{eq}})}{\pi^2 \omega^2 I_{\text{in}}}}. \tag{31}$$

Mutual inductance $M$ can be estimated online according to the algorithm shown in Fig. 10, where $V_0$, $I_0$, $V_{\text{in}}$, and $I_{\text{in}}$ are dc signals and can be sampled easily. $\theta_1$ and $R_{\text{eq}}$ can be obtained by (12) and (24) with the initial value $M$, and $\varphi_1$ can be obtained by (14). Finally, the estimation of the mutual inductance $M$ can be achieved by (31).

### *E. Control Strategy*

There are four variables ($\theta_1$, $\theta_2$, $\alpha_1$, and $\alpha_2$) that have been used as control variables in this article. The pulsewidths $\theta_1$ and $\theta_2$ regulate the output voltage and the resistance of equivalent ac load, respectively. The phase angle of the SCC $\alpha_1$ and $\alpha_2$ produce ZVS for the inverter and modulate the resonance of the receiver, respectively. Fig. 11 shows the control block of the proposed method. The blue and the green closed loops are used to modulate the SCCs for efficiency optimization, and the red closed loops are applied to regulate the output voltage. In order to achieve maximum efficiency point, the yellow closed loop is used to track the OLR $R_{\text{eq}}^{\text{opt}}$.

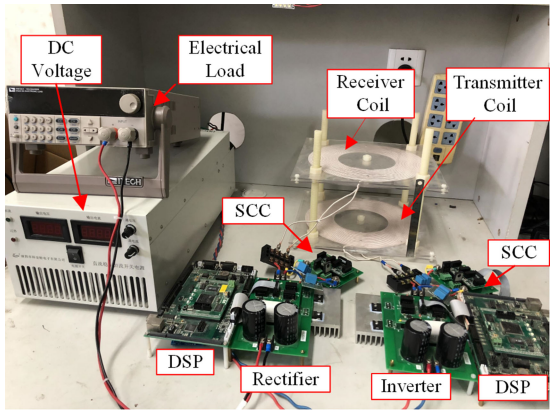


Fig. 12. Prototype of the WPT system.

TABLE II
EXPERIMENTAL PARAMETERS

| Symbol | Parameter | Value |
|---|---|---|
| $V_{in}$ | Input Voltage | 100 V |
| $f$ | Operating frequency | 100 kHz |
| $L_1$ | Inductance of transmitter coil | 99.89 $\mu$H |
| $L_2$ | Inductance of receiver coil | 100.02 $\mu$H |
| $R_1$ | ESR of transmitter side | 0.25 $\Omega$ |
| $R_2$ | ESR of receiver side | 0.27 $\Omega$ |
| $C_s$ | Series capacitor | 42 nF |
| $C_a$ | SCC capacitor | 42 nF |
| $C_0$ | Output capacitor | 470 $\mu$F |

## IV. IMPLEMENTATION

### *A. Prototype*

A 650-W prototype of the WPT system with dual active bridges is implemented to verify feasibility and demonstrate the proposed control strategy. The prototype is shown in Fig. 12 and the parameters are shown in Table II. Two digital signal processors (TMS320F28335) are used as the controller. The information exchange between two controllers is implemented

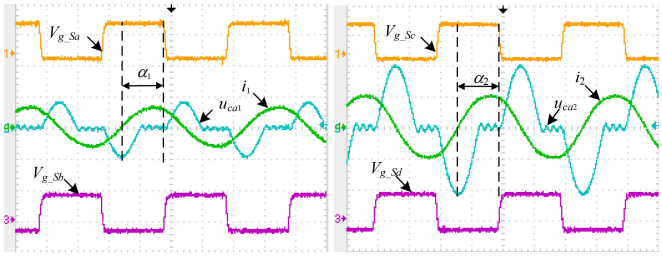


Fig. 13. Experimental results of SCC operation. (a) Transmitter side. (b) Receiver side ($V_{g\_Sa}$, $V_{g\_Sb}$, $V_{g\_Sc}$, $V_{g\_Sd}$: 20 V/div, $i_1$, $i_2$: 25 A/div, $u_{ca1}$, $u_{ca2}$: 50 V/div).

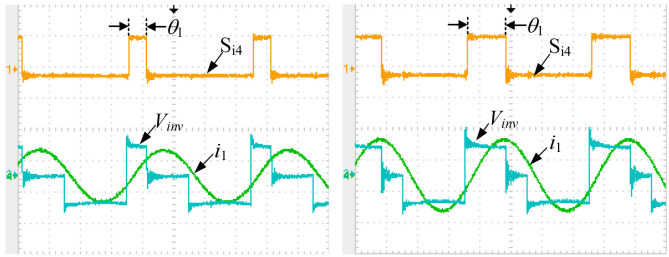


Fig. 14. Inverter operation. (a) $\theta_1 = \pi/6$. (b) $\theta_1 = \pi/3$ ($S_{i4}$: 20 V/div, $i_1$: 25 A/div, $V_{\rm inv}$: 50 V/div).

by wireless communication with RF modules (nRF24L01). The phase angle of the SCC should be regulated according to the current zero-crossing point in order to achieve variable capacitance. Therefore, the current zero-crossing detection circuit is adopted. In order to compensate the possible position deviations between the transmitter and receiver coils, the estimation of the mutual inductance $M$ is implemented on the transmitter side.

As mentioned above, a symmetrical structure is implemented, and the same parameters of the components in the transmitter and receiver side are adopted, which can greatly simplify the design. The initial distance of the transmitter and the receiver coils is 150 mm. N-channel SiC MOSFET (C3M0065090D) with typical on-resistance 65 m$\Omega$ is chosen for the inverter and the rectifier. In addition, the fast-recovery diode (DSEI 2X61-02A) is used as the uncontrolled rectifier for comparison with the active rectifier. It should be noted that the same low on-resistance MOSFET is applied to the SCC, so the power losses in the SCC are minimized.

Each SCC PWM signal is modulated with the zero-crossing signal of the current in the corresponding side. The isolated driver is required for each MOSFET in SCC because the source node of the MOSFET is connected to a floating node. In this article, the gate drive optocoupler (ACPL-W349) is selected for the isolated drivers. It is important to point out that the accuracy of zero-crossing detection might affect the system performance. The high-bandwidth, low-time-delay current sensors and comparators should be used to ensure a good accuracy of the zero-crossing detection. In this article, the current frequency is 100 kHz (corresponding to 10 $\mu$s cycle), and the detection delay of the zero crossing is very small (approximately 80 ns). Then, the zero-crossing detection delay is negligible in the proposed implementation, which has been verified by the experimental results.

### B. Experimental Results

Fig. 13 shows the experimental waveforms of the SCC, where $i_1$ and $i_2$ are the resonant current in the transmitter side and the receiver side, respectively, $V_{g\_Sa}$ and $V_{g\_Sb}$ are gating signals of the SCC in transmitter side, $V_{g\_Sc}$ and $V_{g\_Sd}$ are the gating signals of the SCC in the receiver side, $u_{ca1}$ and $u_{ca2}$ are the capacitor voltages of the SCC in the transmitter and receiver sides, respectively. Fig. 13(a) shows the SCC operation of the transmitter side by setting $Q = 5$. Giving that the phase angle shift $\alpha_1$ is 106.2°, an inductive load is exerted to the inverter, which can achieve the ZVS operation. Fig. 13(b) shows the SCC operation of receiver side. It is shown that the phase angle shift $\alpha_2$ is 113.1° and the value of $C_{\rm eq2}$ is adjusted to the resonant frequency point in receiver side.

TABLE III
EXPERIMENTAL RESULTS OF THE MUTUAL INDUCTANCE $M$ ESTIMATION

| Distance (face-to-face) | Mutual Inductance M | Estimated $M$ |
|---|---|---|
| 10 cm | 19.20 $\mu$H | 18.82 $\mu$H |
| 12cm | 14.81 $\mu$H | 15.02 $\mu$H |
| 14 cm | 11.40 $\mu$H | 11.26 $\mu$H |
| 16 cm | 8.95 $\mu$H | 8.82 $\mu$H |
| 18 cm | 6.88 $\mu$H | 6.42 $\mu$H |
| 20 cm | 5.61 $\mu$H | 5.38 $\mu$H |

Fig. 14 shows the inverter operation under different pulsewidth $\theta_1$. During a switching cycle, the conduction time of switches, $S_{i1}$ and $S_{i2}$, lasts about 5 $\mu$s, while the conduction time of $S_{i4}$ adjusts by controlling $\theta_1$. As shown in Fig. 14(a) and (b), the conduction time of $S_{i4}$ are 1.67 and 3.33 $\mu$s for $\theta_1$ being $\pi/6$ and $\pi/3$, respectively. Fig. 14(a) and (b) shows that the current $i_1$ changes from negative to positive when switch $S_{i4}$ is turned ON, implying that $i_1$ flows through the antiparallel diode of switch $S_{i4}$. As shown in Fig. 14, the current $i_1$ lags behind the voltage $V_{\rm inv1}$, implying that the inverter has an inductive load. It can be known from Fig. 7 that the inverter performs the ZVS operation.

Table III shows the experimental results of the mutual inductance estimation, where the mutual inductance changes by varying the face-to-face distance between the transmitter and receiver coils. The estimation errors are not large, and the maximum estimation error of mutual inductance is only 6.7%. These experimental results verify the feasibility of the proposed estimation method. It should be noted that the measurement errors can be reduced further by improving the filtering algorithms.

Moreover, the inverter operation is tested by varying the pulsewidth $\theta_1$ with the input voltage $V_{\rm in} = 100$ V. Its corresponding pulsewidth and the output dc voltage $V_0$ are recorded. According to (12), the relationship between the pulsewidth $\theta_1$ and the output dc voltage $V_0$ is calculated (solid line). The experimental results (dotted line) are also elaborated upon in Fig. 15. It shows the experimental results almost completely agree with the analytical results, where the output voltage of the experiment decreases slightly due to the resistance of the circuit.

Adjusting the SCC in the receiver side can completely compensate for the inductive reactance, and the reflected impedance of the receiver side to the transmitter side is pure resistance,

TABLE IV
PERFORMANCE COMPARISONS

| Reference | Operation frequency (kHz) | Distance (cm) | Coupling coefficient | Max. efficiency (%) |
|---|---|---|---|---|
| This article | 100 | 15 | 0.12 | 91.2 |
| [3] @2018 | 30 | 10 | 0.18 | 91.7 |
| [30] @2018 | 85.5 | 3 | 0.15 | 81 |
| [31] @2018 | 917 | 50 | 0.01 | 70 |
| [16] @2018 | 592 | 3.35 | N/A | 73 |
| [19] @2018 | 100 | 5 | 0.168 | 85 |
| [18] @2017 | 6780 | 3 | 0.09 | 51 |

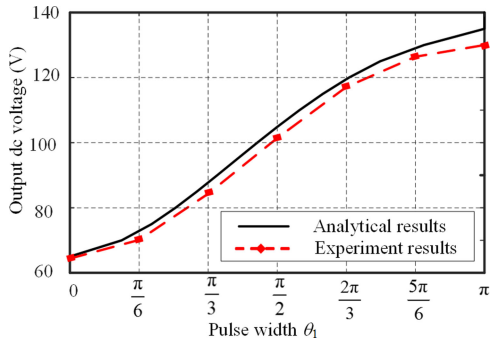


Fig. 15. Voltage regulations in inverter.

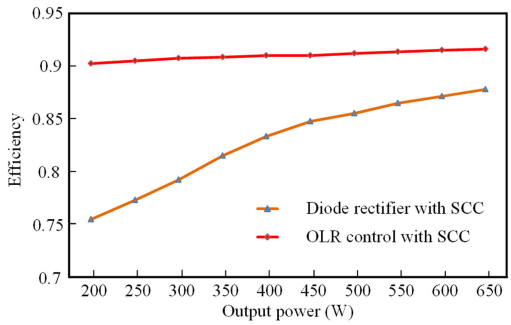


Fig. 17. Efficiency comparisons of OLR control with SCC and diode rectifier.

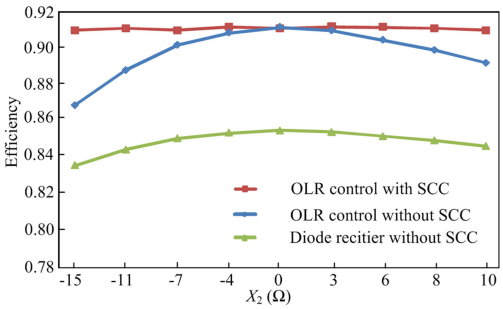


Fig. 16. Comparisons of experimental results in efficiency.

which leads to no changes in the phase between the primary current $i_1$ and output voltage $V_{\text{inv}}$. Fig. 16 shows the experimental results of the efficiency for the OLR control method with SCC, the OLR control method without SCC, and the diode rectifier without SCC, where the output power 500 W. The reactance is completely compensated by adjusting the SCC, then, $X_2$ is 0 and the system obtains the highest efficiency under the OLR control method with SCC. If the SCC is absent, the additional reactance may cause $X_2$ to become nonzero due to the nonresonant condition in the receiver side. Then, the efficiency would be decreased, because the existence of nonzero $X_2$ requires higher apparent power and engenders efficiency degradation. Thus, lager $|X_2|$ results in a smaller overall efficiency in diode rectifier and OLR control without SCC, as shown in Fig. 16. With the OLR control and SCC compensation in simultaneously, the system can obtain efficiency as high as 91.2%.

Fig. 17 shows the overall efficiency of the OLR control and the passive diode rectifier with output power rating from 200 to 650 W. The overall system efficiency of the OLR control with SCC compensation is greater than 90% in all load conditions. Compared to the traditional diode rectifier with SCC compensation, the proposed method can dramatically improve overall system efficiency by about 7% in 650 W and about 15% in 200 W because the OLR control method always adjusts $R_e$ to $R_e^{\text{opt}}$ under various load conditions.

### C. Comparisons

In recent years, it has been reported that different topologies and control methods simultaneously achieve constant voltage/current output and high efficiency tracking. The parameters and the results of the relevant state of the art are listed in Table III. Although all of the topologies and methods adopt converter on the receiver side for efficiency optimization, a fair comparison among the results of their usage is difficult to obtain due to the different system parameters and circuit structures. Table IV shows recent publications that relate to efficiency optimization and constant voltage output for the WPT system, where Hui *et al.* [30] have obviously higher efficiency due to low operation frequency (then small distance) and the high coupling coefficient. This article improves the system efficiency by the SCC to track the maximum efficiency point, which is higher than the efficiency of most of the methods.

## V. CONCLUSION

This article proposes a WPT system with dual SCCs for efficiency optimization. The regulation method and equivalent capacitance of the SCC are introduced. The OAVC control is applied to the active bridge converters for a wide-ranging

soft-switching operation. Four control variables are used to realize the efficiency optimization of the WPT system where the pulsewidth of the inverter is used to regulate the output voltage, the pulsewidth of the rectifier optimizes the equivalent load impedance, the phase angle of the SCC in the transmitter side modulates the load so that it is inductive for the ZVS consideration, and phase angle of the SCC in the receiver side tunes the resonance frequency of the rectifier, which is fixed at the operating frequency. In addition, the online estimation of the mutual inductance based on the input dc signal sampling is put forward for compensating possible position deviation of coils. A 650-W prototype operating at 100 kHz is built to validate the feasibility of the proposed WPT system. The experimental results show that with OAVC control and the SCC regulations, performance and efficiency improvement are good at various loads for the WPT system.

## Appendix I

The SCC is excited by a sinusoidal current

$$i_x = I_x \sin(\omega t) \tag{A1}$$

where $I_x$ is the amplitude of the input current and $\omega$ is the angular frequency of the input current. The voltage of the capacitor $C_a$ is the same as the voltage dropped across Terminals A and B, which is $U_{ab}$. During the period in which the current is flowing through the capacitor, it has

$$C_a \frac{du_{ab}}{dt} = i_{ca}. \tag{A2}$$

In the interval $[\alpha, \alpha + \varphi]$, the charge and discharge of the capacitor $C_a$ can be controlled by regulating the phase angle shift $\alpha$ and the interval angle $\varphi$. Then, the voltage across the capacitor $C_a$ can be expressed as

$$\begin{aligned} u_{ab} &= u(\alpha) + \frac{1}{C_a}\int_{\alpha}^{\omega t} i_{ca} dt \\ &= \frac{I_{ab}}{\omega C_a}[\cos\alpha - \cos(\omega t)]. \end{aligned} \tag{A3}$$

Supposing that $\omega t$ is $\alpha + \varphi$, and $u_{ab}$ is 0 and substituting them into (A3), it has

$$\alpha = \pi - \frac{\phi}{2}. \tag{A4}$$

By applying the Fourier transformation, the amplitude of the fundamental component of voltage $u_{ab}$ is

$$\begin{aligned} U_{ab(1)} &= \frac{2}{\pi}\int_{\alpha}^{\alpha+\phi} u_{ab}\cos(\omega t) d(\omega t) \\ &= \frac{I_{ab}}{\omega}\left[-\left(\frac{2\pi - 2\alpha + \sin 2\alpha}{\pi C_a}\right)\right] = -\frac{I_{ab}}{\omega C_{\rm sc}}. \end{aligned} \tag{A5}$$

From the last two items of (A5), the equivalent capacitance $C_{\rm sc}$ of the SCC can be expressed as

$$C_{\rm sc} = \frac{\pi C_a}{2\pi - 2\alpha + \sin 2\alpha}. \tag{A6}$$

## Appendix II

According to (5), the output voltage across the equivalent load $R_{\rm eq}$ is

$$V_{\rm rec1} = |G_v| \cdot V_{\rm ins1\_rms}. \tag{A7}$$

Since the output power should be balanced, it has

$$\frac{V_{\rm rec1}^2}{R_{\rm eq}} = \frac{V_0^2}{R_L} \tag{A8}$$

where $V_0$ and $R_L$ are dc voltage and the resistance of the load, respectively. Substituting (10) and (A7) into (A8), the desired pulsewidth $\theta_1$ for voltage regulation can be

$$\begin{aligned} \theta_1 = \arccos\Bigg[\frac{1}{3}\Bigg(5 - \frac{\pi^2 V_0^2}{V_{\rm in}^2} \\ \times \frac{\left((R_1(R_2+R_{\rm eq}) + (\omega M)^2\right)^2 + X_1^2(R_2+R_{\rm eq})^2)}{(\omega M)^2 R_{\rm eq} R_L}\Bigg)\Bigg]. \end{aligned} \tag{A9}$$

## References


[1] S. Y. R. Hui, W. Zhong, and C. K. Lee, "A critical review of recent progress in mid-range wireless power transfer," *IEEE Trans. Power Electron.*, vol. 29, no. 9, pp. 4500–4511, Sep. 2014.

[2] T. C. Beh, M. Kato, T. Imura, S. Oh, and Y. Hori, "Automated impedance matching system for robust wireless power transfer via magnetic resonance coupling," *IEEE Trans. Ind. Electron.*, vol. 60, no. 9, pp. 3689–3698, Sep. 2013.

[3] S. Y. R. Hui, W. Zhong, and C. K. Lee, "An active-rectifier-based maximum efficiency tracking method using an additional measurement coil for wireless power transfer," *IEEE Trans. Power Electron.*, vol. 33, no. 1, pp. 716–728, Jan. 2018.

[4] C.-S. Wang, O. H. Stielau, and G. A. Covic, "Design considerations for a contactless electric vehicle battery charger," *IEEE Trans. Ind. Electron.*, vol. 52, no. 5, pp. 1308–1314, Oct. 2005.

[5] J. Sallán, J. L. Villa, A. Llombart, and J. F. Sanz, "Optimal design of ICPT systems applied to electric vehicle battery charge," *IEEE Trans. Ind. Electron.*, vol. 56, no. 6, pp. 2140–2149, Jun. 2009.

[6] C. Liu, K. T. Chau, D. Wu, and S. Gao, "Opportunities and challenges of vehicle-to-home, vehicle-to-vehicle, and vehicle-to-grid technologies," *Proc. IEEE*, vol. 101, no. 11, pp. 2409–2427, 2013.

[7] M. Sugino and T. Masamura, "The wireless power transfer systems using the Class E push-pull inverter for industrial robots," in *Proc. IEEE Wireless Power Transf. Conf.*, May 2017, pp. 1–3.

[8] X. Liu and S. Y. Hui, "Simulation study and experimental verification of a universal contactless battery charging platform with localized charging features," *IEEE Trans. Power Electron.*, vol. 22, no. 6, pp. 2202–2200, Nov. 2007.

[9] D. Ahn and S. Hong, "Wireless power transmission with self-regulated output voltage for biomedical implant," *IEEE Trans. Ind. Electron.*, vol. 61, no. 5, pp. 2225–2235, May 2014.

[10] X. Hu, J. Zhang, S. Xu, and Y. Jiang, "Investigation of a new modular multilevel converter with DC fault blocking capability," *IEEE Trans. Ind. Appl.*, vol. 55, no. 1, pp. 552–562, Jan./Feb. 2019.

[11] J. Zhang, J. Hang, S. Ding, and M. Cheng, "Online diagnosis and localization of high-resistance connection in PMSM with improved fault indicator," *IEEE Trans. Power Electron.*, vol. 32, no. 5, pp. 3585–3594, May 2017.

[12] H. Zeng and F. Z. Peng, "Non-linear capacitor based variable capacitor for self-tuning resonant converter in wireless power transfer," in *Proc. IEEE 33rd Annu. Appl. Power Electron. Conf. Expo.*, 2018, pp. 1375–1379.

[13] C. Karnstedt and C. Buenrostro, "Dynamic tuning in wireless energy transfer systems," U.S. Patent 10141788B2, Nov. 27, 2018.

[14] J. Alonso, M. Perdigão, M. Dalla Costa, S. Zhang, and Y. Wang, "Analysis and experimentation of the quad-U variable inductor for power electronics applications," *IET Power Electron.*, vol. 11, no. 14, pp. 2330–2337, Nov. 27, 2018.

[15] W. Zhang, S. C. Wong, K. T. Chi, and Q. Chen, "Design for efficiency optimization and voltage controllability of series–series compensated inductive power transfer systems," *IEEE Trans. Power Electron.*, vol. 29, no. 1, pp. 191–200, Jan. 2014.
[16] X. Tang, J. Zeng, K. P. Pun, S. Mai, C. Zhang, and Z. Wang, "Low-cost maximum efficiency tracking method for wireless power transfer systems," *IEEE Trans. Power Electron.*, vol. 33, no. 6, pp. 5317–5329, Jun. 2018.
[17] H. Li, J. Li, K. Wang, W. Chen, and X. Yang, "A maximum efficiency point tracking control scheme for wireless power transfer systems using magnetic resonant coupling," *IEEE Trans. Power Electron.*, vol. 30, no. 7, pp. 3998–4008, Jul. 2015.
[18] T. Yeo, D. Kwon, S. Khang, and J. Yu, "Design of maximum efficiency tracking control scheme for closed-loop wireless power charging system employing series resonant tank," *IEEE Trans. Power Electron.*, vol. 32, no. 1, pp. 471–478, Jan. 2017.
[19] X. Dai, X. Li, Y. Li, and P. Hu, "Maximum efficiency tracking for wireless power transfer systems with dynamic coupling coefficient estimation," *IEEE Trans. Power Electron.*, vol. 33, no. 6, pp. 5005–5015, Jun. 2018.
[20] W. Zhong and S. Y. R. Hui, "Maximum energy efficiency operation of series-series resonant wireless power transfer systems using on-off keying modulation," *IEEE Trans. Power Electron.*, vol. 33, no. 4, pp. 3595–3603, Apr. 2018.
[21] B. Peschiera, K. Aditya, and S. S. Williamson, "Asymmetrical voltage-cancellation control for a series-series fixed-frequency inductive power transfer system," in *Proc. IEEE 40th Annu. Conf. Ind. Electron. Soc.*, 2014, pp. 2971–2977.
[22] H. Wu, T. Mu, H. Ge, and Y. Xing, "Full-range soft-switching-isolated buck-boost converters with integrated interleaved boost converter and phase-shifted control," *IEEE Trans. Power Electron.*, vol. 31, no. 2, pp. 987–999, Feb. 2016.
[23] B. Zhao, Q. Song, and W. Liu, "Power characterization of isolated bidirectional dual-active-bridge DC–DC converter with dual-phase-shift control," *IEEE Trans. Power Electron.*, vol. 27, no. 9, pp. 4172–4176, Sep. 2012.
[24] M. Qiu, K. J. Praveen, and H. Zhang, "An APWM resonant inverter topology for high frequency AC power distribution systems," *IEEE Trans. Power Electron.*, vol. 19, no. 1, pp. 121–129, Jan. 2004.
[25] W. J. Gu and K. Harada, "A new method to regulate resonant converters," *IEEE Trans. Power Electron.*, vol. 3, no. 4, pp. 430–439, Oct. 1988.
[26] Z. Hu, Y. Qiu, and Y. F. Liu, "Digital implementation of load sharing method for interleaved LLC converters," in *Proc. Control Model. Power Electron.*, 2013, pp. 1–7.
[27] Z. Hu, Y. Qiu, L. Wang, and Y. F. Liu, "An interleaved LLC resonant converter operating at constant switching frequency," *IEEE Trans. Power Electron.*, vol. 29, no. 6, pp. 2931–2943, Jun. 2014.
[28] D. Kim and D. Ahn, "Self-tuning LCC inverter using PWM-controlled switched capacitor for inductive wireless power transfer," *IEEE Trans. Ind. Electron.*, vol. 66, no. 5, pp. 3983–3992, May 2018.
[29] J. Osawa, T. Isobe, and H. Tadano, "Efficiency improvement of high frequency inverter for wireless power transfer system using a series reactive power compensator," in *Proc. IEEE 12th Int. Conf. Power Electron. Drive Syst.*, 2017, pp. 992–998.
[30] S. Y. R. Hui, W. Zhong, and C. K. Lee, "Constant current charging and maximum efficiency tracking control scheme for supercapacitor wireless charging," *IEEE Trans. Power Electron.*, vol. 33, no. 10, pp. 9088–9100, Oct. 2018.
[31] H. Li, J. Fang, S. Chen, K. Wang, and Y. Tang, "Pulse density modulation for maximum efficiency point tracking of wireless power transfer systems," *IEEE Trans. Power Electron.*, vol. 33, no. 6, pp. 5492–5501, Jun. 2018.

**Jianzhong Zhang** (M'08–SM'16) received the M.Sc. and Ph.D. degrees in electrical engineering from Southeast University, Nanjing, China, in 2005 and 2008, respectively.

From 2006 to 2007, he was a Visiting Scholar with the Department of Energy Technology, Aalborg University, Aalborg, Denmark. Since 2008, he has been with Southeast University, where he is currently a Research Professor with the School of Electrical Engineering. He was a Visiting Professor with the Worcester Polytechnic Institute, Worcester, USA, and the University of British Columbia, Vancouver, Canada, in July 2012 and August 2017, respectively. His research interests include power electronics, electrical machines, and renewable power generation.

Dr. Zhang is a recipient of the Institution Premium Award at the Institutions of Engineering and Technology, U.K.

**Jin Zhao** (S'16) received the M.Sc. degree in electrical engineering from the Jiangsu University of Science and Technology, Zhenjiang, China, in 2014. He is currently working toward the Ph.D. degree with the Department of Electrical Engineering, Southeast University, Nanjing, China.

Since December 2018, he has been with The University of British Columbia, Vancouver, BC, Canada, where he is currently a Joint Ph.D. Student with the Electrical Power and Energy Systems (EPES) Research Group, Faculty of Applied Science. His research interests include resonant power converters, wireless power transfer, and electric machines and drives.

**Yaqian Zhang** (S'18) received the B.Eng. degree from the University of Electronic Science and Technology of China, Chengdu, China, in 2016. She is currently working toward the Ph.D. degree with the School of Electrical Engineering, Southeast University, Nanjing, China.

Her research focuses on the control, efficiency, and power density improvements of large power converters including modular multilevel converter (MMC) and the solid-state transformer based on MMC.

**Fujin Deng** (SM'19) received the B.Eng. degree in electrical engineering from the China University of Mining and Technology, Jiangsu, China, in 2005, the M.Sc. degree in electrical engineering from Shanghai Jiao Tong University, Shanghai, China, in 2008, and the Ph.D. degree in energy technology from Aalborg University, Aalborg, Denmark, in 2012.

He joined the Southeast University in 2017 and was a Professor with the School of Electrical Engineering, Southeast University, Nanjing, China. From 2013 to 2015 and from 2015 to 2017, he was a Postdoctoral Researcher and an Assistant Professor, respectively, with the Department of Energy Technology, Aalborg University, Aalborg, Denmark. His main research interests include wind power generation, multilevel converters, high-voltage direct-current technology, dc grid, and offshore wind farm-power systems dynamics.